Journal of Materials Chemistry A

ROYAL SOCIETY OF CHEMISTRY

PAPER

View Article Online
View Journal | View Issue

Cite this: J. Mater. Chem. A, 2022, 10, 9941

Enhanced oxygen redox reversibility and capacity retention of titanium-substituted $Na_{4/7}[\square_{1/7}Ti_{1/7}Mn_{5/7}]O_2$ in sodium-ion batteries†

Stephanie F. Linnell, [ab] Eun Jeong Kim, [ab] Yong-Seok Choi, [bcd] Moritz Hirsbrunner,[e] Saki Imada, [f] Atin Pramanik, [a] Aida Fuente Cuesta,[a] David N. Miller, [a] Edoardo Fusco,[a] Bela E. Bode, [a] John T. S. Irvine, [ab] Laurent C. Duda, [e] David O. Scanlon [bcd] and A. Robert Armstrong *[ab]

Anion redox reactions offer a means of enhancing the capacity of layered sodium transition metal oxide positive electrode materials. However, oxygen redox reactions typically show limited reversibility and irreversible structural changes upon cycling, resulting in rapid capacity loss. Here, the Ti-substituted $Na_{4/7}[\square_{1/7}Ti_{1/7}Mn_{5/7}]O_2$ (where $\square$ represents a transition metal vacancy) is presented as a positive electrode material for sodium-ion batteries. $Na_{4/7}[\square_{1/7}Ti_{1/7}Mn_{5/7}]O_2$ delivers a reversible capacity of 167 mA h g^{-1} after 25 cycles at 10 mA g^{-1} within the voltage range of 1.6–4.4 V and presents enhanced stability compared with $Na_{4/7}[\square_{1/7}Mn_{6/7}]O_2$ over the voltage range 3.0–4.4 V. The structural and electronic structural changes of this Ti^{4+} substituted phase are investigated by powder X-ray diffraction, X-ray absorption spectroscopy, electron paramagnetic resonance and Raman spectroscopy, supported by density functional theory calculations. These results show that the $Na_{4/7}[\square_{1/7}Mn_{6/7}]O_2$ structure is maintained between 3.0 and 4.4 V, and the presence of TiO_6 octahedra in $Na_{4/7}[\square_{1/7}Ti_{1/7}Mn_{5/7}]O_2$ relieves structural distortions from Jahn–Teller distorted $Mn^{3+}O_6$ between 1.6 and 4.4 V. Furthermore, Ti^{4+} substitution stabilises the adjacent O 2p orbitals and raises the ionicity of the Mn–O bonds, increasing the operating potential of $Na_{4/7}[\square_{1/7}Ti_{1/7}Mn_{5/7}]O_2$. Thereby providing evidence that the improved electrochemical performance of $Na_{4/7}[\square_{1/7}Ti_{1/7}Mn_{5/7}]O_2$ can be attributed to Ti^{4+} substitution. This work provides insight and strategies for improving the structural stability and electrochemical performance of sodium layered oxides.

Received 23rd February 2022
Accepted 30th March 2022

DOI: 10.1039/d2ta01485h

rsc.li/materials-a

1. Introduction

The limited availability and hence the high-cost of raw materials used in lithium-ion batteries (LIBs) has driven research towards alternative rechargeable battery technologies. Among these, sodium-ion batteries (SIBs) have attracted considerable attention as a viable replacement to LIBs for large-scale applications, such as grid energy storage because of the low-cost, high-abundance and uniform geographical distribution of sodium.[1,2] However, one of the main challenges to overcome is the development of high energy density positive electrode materials for the practical application of SIBs.[3–6]

The use of both cation and anion redox couples has become a promising method to enhance the capacity of positive electrode materials, thereby increasing the energy density of batteries. Lithium-rich layered oxides ($Li_{1+x}M_{1-x}O_2$, M = transition metal), have been widely-studied and are promising positive electrode materials for lithium-ion batteries (LIBs).[7–9] For instance, $Li_{1.20}Mn_{0.54}Co_{0.13}Ni_{0.13}O_2$ in which lithium atoms are situated in the transition metal layer, delivers an extraordinarily high capacity, attributed to the cumulative use of transition metal and oxygen redox couples.[10–12] However, materials that exhibit oxygen redox generally show large voltage hysteresis during the initial charge/discharge cycles, because of irreversible structural changes including cation migration from the transition metal layers, resulting in the release of molecular O_2 and thus, rapid capacity fade.[7,13–15] Alternatively, some sodium-based transition metal layered oxides, $Na_xM_yO_2$, have shown suppressed cation migration

[a]School of Chemistry, University of St Andrews, St Andrews, Fife, KY16 9ST, UK. E-mail: ara@st-andrews.ac.uk

[b]The Faraday Institution, Quad One, Harwell Science and Innovation Campus, Didcot, OX11 0RA, UK

[c]Department of Chemistry, University College London, 20 Gordon Street, London, WC1H 0AJ, UK

[d]Thomas Young Centre, University College London, Gower Street, London WC1E 6BT, UK

[e]Department of Physics and Astronomy, Division of Molecular and Condensed Matter Physics, Uppsala University, Uppsala, S-75120, Sweden

[f]Faculty of Electrical Engineering and Electronics, Kyoto Institute of Technology, Sakyo, Kyoto 606-8585, Japan

† Electronic supplementary information (ESI) available. See DOI: 10.1039/d2ta01485h

owing to the increased ionic size difference between sodium and the transition metal.[16–20] One sodium-based layered material that exhibits stable oxygen anion redox is $Na_{4/7}[\square_{1/7}Mn_{6/7}]O_2$. The transition metal vacancies in $Na_{4/7}[\square_{1/7}Mn_{6/7}]O_2$ (where $\square$ represents a transition metal vacancy) and the unique ordering between vacancies and manganese, generates O 2p nonbonding orbitals, promoting reversible oxygen redox activity.[21] $Na_{4/7}[\square_{1/7}Mn_{6/7}]O_2$ maintains the layered structure over several cycles without migration of Mn cations and preserves the ABBCCA oxygen stacking sequence.[22,23] As a result, $Na_{4/7}[\square_{1/7}Mn_{6/7}]O_2$ exhibits more reversible anion redox compared with other sodium-based oxygen redox active materials with negligible voltage hysteresis and can deliver a high specific capacity of up to $\sim$200 mA h g^{-1}, thereby demonstrating the importance of vacancies in stabilising anion redox.[21,24,25]

Despite the good reversibility of $Na_{4/7}[\square_{1/7}Mn_{6/7}]O_2$ reported to date, its long-term cycle life remains questionable. This is especially true when both cation and anion redox reactions are utilised, where $Na_{4/7}[\square_{1/7}Mn_{6/7}]O_2$ undergoes a continuous capacity fade from $\sim$200 to $\sim$125 mA h g^{-1} over 60 cycles.[21,25] To promote reversible redox reactions, an effective strategy is through doping with transition metals. Among the dopants studied, Ti-substituted materials have drawn attention in recent years due to the low-cost, chemical stability and wide-spread distribution in the earth's crust. Yoshida *et al.* revealed that substituting Mn with Ti in P2-type $Na_{2/3}Ni_{1/3}Mn_{2/3-x}Ti_xO_2$, enhanced the cycling performance and increased average discharge voltage to 3.7 V. Moreover, increasing the amount of Ti-substitution resulted in a smoother voltage profile, possibly because of the suppression of the P2 $\rightarrow$ O2 phase transition.[26] Li *et al.* demonstrated that Ti^{4+} substitution reduced the Li^+/Mn^{4+} ordering for $Na_{0.72}Li_{0.24}Ti_{0.10}Mn_{0.66}O_2$ which enhanced the reversibility of the oxygen redox process and resulted in a superior reversible capacity of 165 mA h g^{-1} over 80 cycles.[27] These results show that Ti-substitution is a proven method to stabilise the structure, smooth the charge/discharge profile, elevate the working potential, and improve the cycling stability.[26–28]

Liu *et al.*, have recently reported a superior cycling stability of 79% for $Na_{4/7}[\square_{1/7}Ti_{1/7}Mn_{5/7}]O_2$ compared with 17% for $Na_{4/7}[\square_{1/7}Mn_{6/7}]O_2$ within 1.5–4.6 V at 50 mA g^{-1}, negligible volume change (0.11%) during charge/discharge and no irreversible O_2 evolution upon charge to 4.6 V.[29] The present study aims to understand the role of Ti-substitution on the charge compensation mechanism of $Na_{4/7}[\square_{1/7}Mn_{6/7}]O_2$. Herein, we report that Ti-substituted $Na_{4/7}[\square_{1/7}Ti_{1/7}Mn_{5/7}]O_2$ shows a remarkable improvement over $Na_{4/7}[\square_{1/7}Mn_{6/7}]O_2$ for both cation and anion redox stability: for a wide voltage range (1.6–4.4 V) over which both cation (Mn^{3+}/Mn^{4+}) and anion (O^{2-}/O_2^{n-}) redox reactions are activated, $Na_{4/7}[\square_{1/7}Ti_{1/7}Mn_{5/7}]O_2$ delivers higher operating potential, reversible capacity (167 mA h g^{-1}), and greater capacity retention of 88% than $Na_{4/7}[\square_{1/7}Mn_{6/7}]O_2$ with a lower reversible capacity of 143 mA h g^{-1} and capacity retention of 76% after 25 cycles at 10 mA g^{-1}. Additional electrochemical tests performed for $Na_{4/7}[\square_{1/7}Ti_{1/7}Mn_{5/7}]O_2$ over the voltage range 3.0–4.4 V revealed a highly reversible oxygen redox process with no capacity loss after 50 cycles at 10 mA g^{-1}. We evaluated the changes in the crystal structure and the electronic structure upon cycling using a combination of spectroscopic techniques, together with DFT calculations to determine the redox mechanism and the effects of Ti-substitution on the electrochemical performance. This work on $Na_{4/7}[\square_{1/7}Ti_{1/7}Mn_{5/7}]O_2$, which has the oxygen stacking (ABBCCA) characteristic of P3-type structures extends our survey of P3-type sodium-based layered oxides, and our understanding of the importance of transition metal dopants on stabilising oxygen anion redox.[30–32]

2. Results and discussion

2.1. Structure and electrochemical properties

$Na_{4/7}[\square_{1/7}Mn_{6/7}]O_2$ and $Na_{4/7}[\square_{1/7}Ti_{1/7}Mn_{5/7}]O_2$ were synthesised by a solid-state method.[25] The synchrotron PXRD pattern of as-synthesised $Na_{4/7}[\square_{1/7}Ti_{1/7}Mn_{5/7}]O_2$ can be indexed to a triclinic lattice with space group $P\bar{1}$. The Rietveld refinement of the $Na_{4/7}[\square_{1/7}Mn_{6/7}]O_2$ model using synchrotron PXRD data for $Na_{4/7}[\square_{1/7}Ti_{1/7}Mn_{5/7}]O_2$ is shown in Fig. 1(a) and the results are given in Table S1.† Similarly, the diffraction peaks of the laboratory PXRD pattern of as-synthesised $Na_{4/7}[\square_{1/7}Mn_{6/7}]O_2$ can be indexed using the same model ($P\bar{1}$), as shown in Fig. S1(a),† consistent with previous reports.[21,22,25] The structure of $Na_{4/7}[\square_{1/7}Mn_{6/7}]O_2$ consists of one Na^+ ion (Na1) which occupies distorted prismatic sites above and below the vacant Mn sites, and the other Na^+ ion (Na2) occupies distorted octahedral sites, the Mn^{4+} ions occupy octahedral sites with distorted P3-type oxygen stacking (ABBCCA), as shown in Fig. 1(b). As for Ti-substituted $Na_{4/7}[\square_{1/7}Ti_{1/7}Mn_{5/7}]O_2$, the Ti^{4+} ions can occupy any one of the three Mn sites, as confirmed by calculations which found negligible energy difference between the three Mn sites (see ESI for more details, Fig. S2†). Furthermore, the position of the (001) diffraction peak which relates to the interlayer distance between the transition metal oxide layers is compared in Fig. S3.† The (001) diffraction peak for $Na_{4/7}[\square_{1/7}Ti_{1/7}Mn_{5/7}]O_2$ shifts towards a lower angle. This corresponds to a greater interlayer separation of 5.569 Å for $Na_{4/7}[\square_{1/7}Ti_{1/7}Mn_{5/7}]O_2$, compared with 5.534 Å for $Na_{4/7}[\square_{1/7}Mn_{6/7}]O_2$, as a result of the partial substitution of Ti^{4+} for Mn^{4+} ions, because of the larger ionic radius of Ti^{4+} (0.605 Å) compared with Mn^{4+} (0.53 Å).[33]

The morphology of $Na_{4/7}[\square_{1/7}Ti_{1/7}Mn_{5/7}]O_2$ was examined by SEM. Fig. 1(b) is representative of $Na_{4/7}[\square_{1/7}Ti_{1/7}Mn_{5/7}]O_2$ and shows a homogeneous morphology with agglomerated primary particle size of roughly 100 nm. As-synthesised $Na_{4/7}[\square_{1/7}Mn_{6/7}]O_2$ displays a similar morphology to $Na_{4/7}[\square_{1/7}Ti_{1/7}Mn_{5/7}]O_2$ (Fig. S1(b)†), showing that there is no obvious change in the morphology for the Ti-substituted sample compared with the parent material. EDS elemental maps of $Na_{4/7}[\square_{1/7}Ti_{1/7}Mn_{5/7}]O_2$ are given in Fig. 1(c) and show uniform distribution of Na, Mn, Ti and O. Furthermore, the stoichiometries of Mn and Ti (normalised to Mn + Ti = 6/7) were determined by EDS analysis averaged across several regions to be 0.72 and 0.14, respectively, and close to the expected stoichiometry. This stoichiometry ratio of

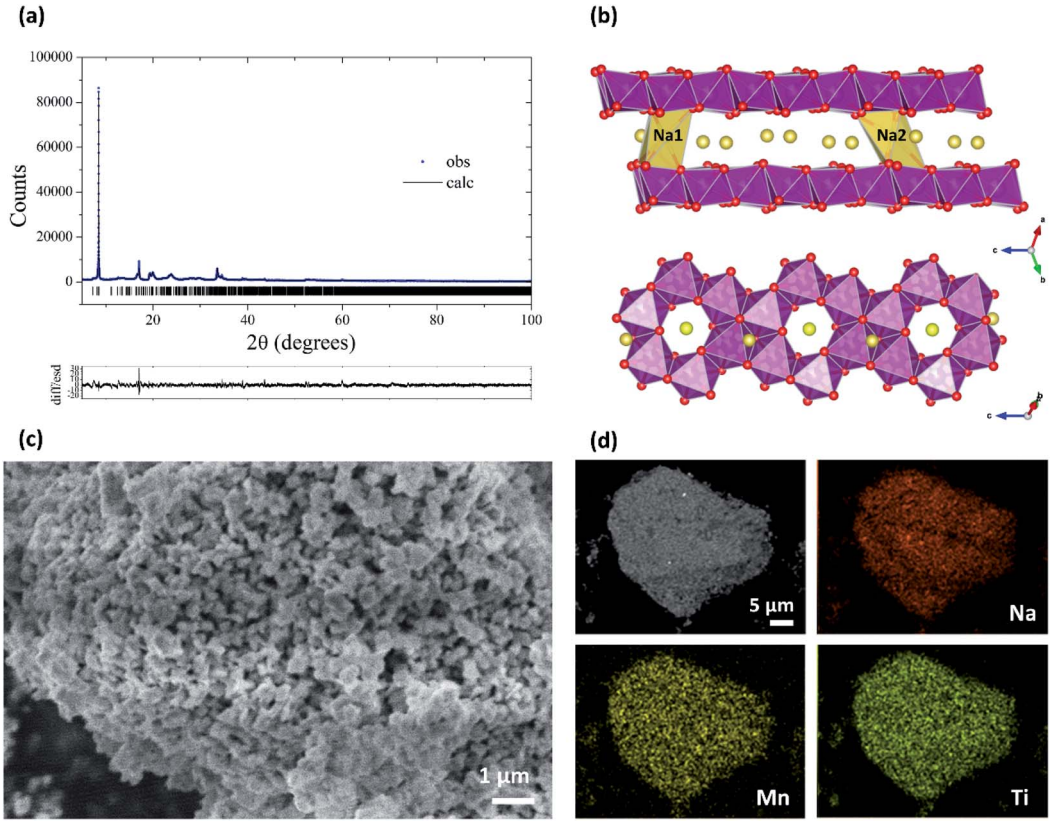

Fig. 1 (a) Synchrotron X-ray Rietveld fit of as-synthesised $Na_{4/7}[\square_{1/7}Ti_{1/7}Mn_{5/7}]O_2$. Observed data points are shown in blue, with fitted profile in black. Tick marks indicate allowed reflections. (b) Refined structural model of $Na_{4/7}[\square_{1/7}Ti_{1/7}Mn_{5/7}]O_2$ with Na^+ ions shown as yellow spheres, Mn as purple polyhedra, Ti shown in white and O as red spheres. The top image shows the alternating layers of Na^+ ions and $[\square_{1/7}Ti^{4+}{}_{1/7}Mn^{4+}{}_{5/7}]$ layers. The Na1 ions occupy distorted prismatic sites and Na2 ions occupy distorted octahedral sites. The bottom image shows the Mn vacancies in the $[\square_{1/7}Ti^{4+}{}_{1/7}Mn^{4+}{}_{5/7}]$ layer. (c) SEM micrograph and (d) EDS mapping of as-synthesised $Na_{4/7}[\square_{1/7}Ti_{1/7}Mn_{5/7}]O_2$.

Mn and Ti corresponds to the solubility limit of Ti in $Na_{4/7}[\square_{1/7}Ti_xMn_{6/7-x}]O_2$ at the synthesis temperature of 600 °C, indicating that the maximum amount of Ti (x) is substituted in $Na_{4/7}[\square_{1/7}Mn_{6/7}]O_2$ (see Fig. S4–S6 and Tables S2–S4 in ESI† for the detailed procedures for the Ti solubility limit calculations).

The electrochemical performance of $Na_{4/7}[\square_{1/7}Ti_{1/7}Mn_{5/7}]O_2$ and $Na_{4/7}[\square_{1/7}Mn_{6/7}]O_2$ was evaluated in sodium-half cells, cycled galvanostatically between 1.6 and 4.4 V at a current rate of 10 mA g^{-1}. Fig. 2(a) and (b) presents the galvanostatic charge/discharge profiles and the corresponding differential capacity *versus* voltage (dQ/dV) plots, respectively, collected for the first cycle of $Na_{4/7}[\square_{1/7}Ti_{1/7}Mn_{5/7}]O_2$ and $Na_{4/7}[\square_{1/7}Mn_{6/7}]O_2$. The materials exhibit similar charge/discharge profiles (Fig. 2(a)) for the first cycle. $Na_{4/7}[\square_{1/7}Mn_{6/7}]O_2$ delivers an initial charge capacity of 63.7 mA h g^{-1}, corresponding to the removal of 0.22 Na^+ ions. It shows a reversible plateau at around 4.20 V, observed in the dQ/dV plot (Fig. 2(b)) as sharp oxidation and reduction peaks at 4.22 and 4.18 V, respectively, based on oxygen redox, which is consistent with data previously reported for $Na_{4/7}[\square_{1/7}Mn_{6/7}]O_2$.[21,22] On discharge to 1.6 V, $Na_{4/7}[\square_{1/7}Mn_{6/7}]O_2$ delivers a discharge capacity of 189.9 mA h g^{-1} equivalent to the insertion of 0.65 Na^+ ions, and exhibits a long, flat discharge plateau at 2.10 V associated with the Mn^{4+}/Mn^{3+} redox couple.[21]

As for $Na_{4/7}[\square_{1/7}Ti_{1/7}Mn_{5/7}]O_2$, Fig. 2(b) shows it delivers an initial charge capacity of 94.9 mA h g^{-1}, equivalent to the extraction of 0.32 Na^+, and exhibits a discharge capacity of 189.9 mA h g^{-1} corresponding to the insertion of 0.65 Na^+. Fig. 2(b) reveals oxidation and reduction peaks, at higher potentials of 4.28 and 4.24 V, respectively, for the oxygen redox process, and a reduction peak at a higher potential of 2.12 V for the Mn^{4+}/Mn^{3+} redox couple for $Na_{4/7}[\square_{1/7}Ti_{1/7}Mn_{5/7}]O_2$. To confirm the higher working potential of $Na_{4/7}[\square_{1/7}Ti_{1/7}Mn_{5/7}]O_2$, cyclic voltammograms were collected for both materials between 1.6 and 4.4 V at a scan rate of 30 μV s^{-1} and these data are compared in Fig. 2(c). The cyclic voltammograms are consistent with the dQ/dV plots (Fig. 2(b)), showing $Na_{4/7}[\square_{1/7}Ti_{1/7}Mn_{5/7}]O_2$ operates at a higher potential (4.31 and 4.23 V) to $Na_{4/7}[\square_{1/7}Mn_{6/7}]O_2$ (4.28 and 4.16 V). Furthermore, Fig. 2(d) compares the galvanostatic cycling performance of $Na_{4/7}[\square_{1/7}Mn_{6/7}]O_2$ and $Na_{4/7}[\square_{1/7}Ti_{1/7}Mn_{5/7}]O_2$, cycled between 1.6 and 4.4 V at rates of 10 and 100 mA g^{-1}. The discharge capacity of $Na_{4/7}[\square_{1/7}Mn_{6/7}]O_2$ fades rapidly on cycling with only 62 and 44% of the initial discharge capacity retained at 10 and 100 mA g^{-1}, respectively, after 50 cycles. This agrees with earlier work on $Na_{4/7}[\square_{1/7}Mn_{6/7}]O_2$ by de Boisse *et al.* which reported similar cycling performance.[21] By contrast, $Na_{4/7}[\square_{1/7}Ti_{1/7}Mn_{5/7}]O_2$ reveals superior cycling stability at 10 and 100 mA g^{-1},

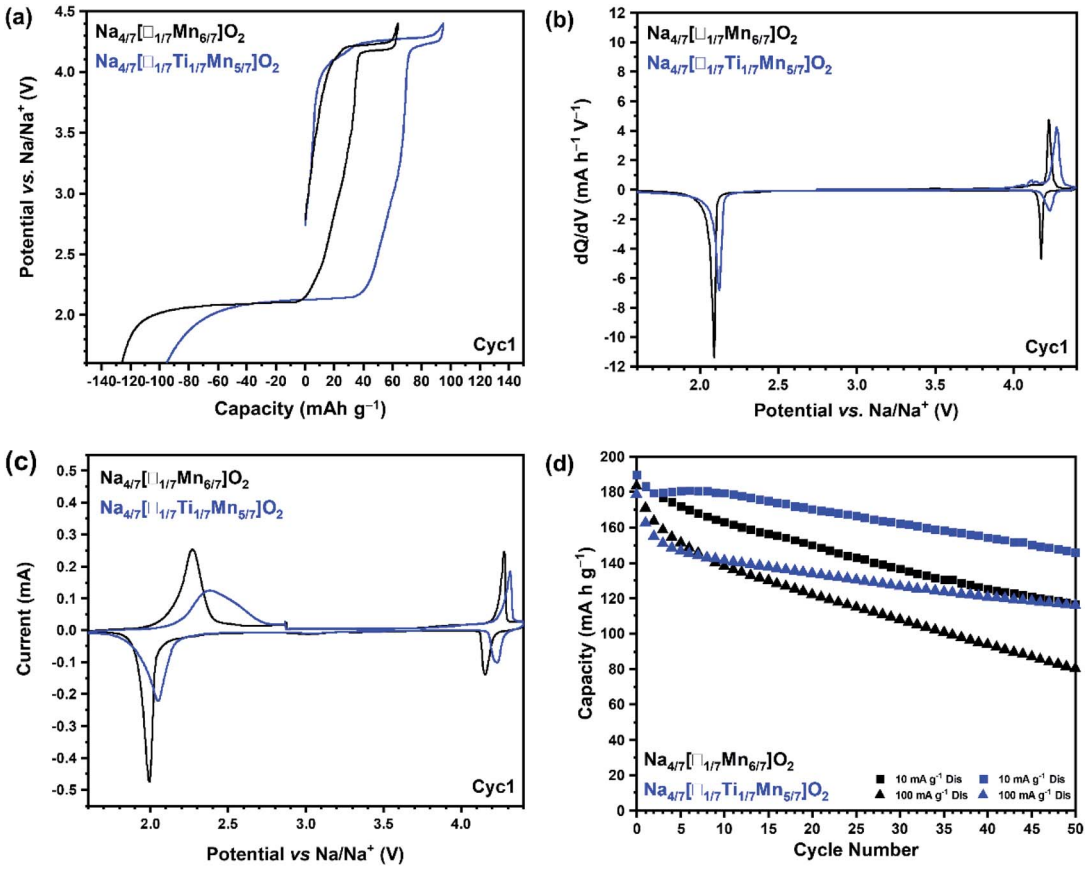

Fig. 2 (a) Galvanostatic charge/discharge curves of the first cycle for $Na_{4/7}[\square_{1/7}Mn_{6/7}]O_2$ (black) and $Na_{4/7}[\square_{1/7}Ti_{1/7}Mn_{5/7}]O_2$ (blue) cycled within the voltage range 1.6–4.4 V at a current rate of 10 mA g^{-1} at 30 °C and (b) the corresponding differential capacity *versus* voltage d*Q*/d*V* plots. (c) Voltammetric analysis of $Na_{4/7}[\square_{1/7}Mn_{6/7}]O_2$ (black) and $Na_{4/7}[\square_{1/7}Ti_{1/7}Mn_{5/7}]O_2$ (blue) collected at a scan rate of 30 μV s^{-1} at 30 °C using 1 M $NaClO_4$ in propylene carbonate containing 3% fluoroethylene carbonate by weight as electrolyte. (d) Galvanostatic cycling performance of $Na_{4/7}[\square_{1/7}Mn_{6/7}]O_2$ (black) and $Na_{4/7}[\square_{1/7}Ti_{1/7}Mn_{5/7}]O_2$ (blue) cycled within the voltage range 1.6–4.4 V at 30 °C. Square-shaped symbols represent discharge capacities of cells cycled at a rate of 10 mA g^{-1} and triangle-shaped symbols represent discharge capacities of cells cycled at a rate of 100 mA g^{-1}.

maintaining 77% and 65%, respectively, of its initial discharge capacity after 50 cycles, showing that Ti-substitution improves the reversibility and cycling performance, consistent with data reported for $Na_{4/7}[\square_{1/7}Ti_{1/7}Mn_{5/7}]O_2$ by Liu *et al.* and other Ti-substituted materials.[26,27,29,34–41]

In order to separate the effect of Ti-substitution on oxygen anionic redox from the combined cation and anion redox reactions, cells of $Na_{4/7}[\square_{1/7}Mn_{6/7}]O_2$ and $Na_{4/7}[\square_{1/7}Ti_{1/7}Mn_{5/7}]O_2$ were cycled galvanostatically between 3.0 and 4.4 V where only oxygen redox couples become active. Fig. 3(a) and (b) shows the differential capacity *versus* voltage for $Na_{4/7}[\square_{1/7}Mn_{6/7}]O_2$ and $Na_{4/7}[\square_{1/7}Ti_{1/7}Mn_{5/7}]O_2$, respectively, cycled between 3.0 and 4.4 V at a current rate of 10 mA g^{-1} over 50 cycles. Fig. 3(a) shows that on cycling $Na_{4/7}[\square_{1/7}Mn_{6/7}]O_2$ the redox couple at 4.2 V, associated with oxygen redox, is lost after about 30 cycles. Whereas, Fig. 3(b) shows that on cycling $Na_{4/7}[\square_{1/7}Ti_{1/7}Mn_{5/7}]O_2$ the redox couple centred about 4.25 V persists after 50 cycles, thereby demonstrating enhanced oxygen redox stability due to the partial substitution of Ti. Additionally, Fig. 3(c) presents the galvanostatic cycling performance of $Na_{4/7}[\square_{1/7}Mn_{6/7}]O_2$ and $Na_{4/7}[\square_{1/7}Ti_{1/7}Mn_{5/7}]O_2$ cycled between 3.0 and 4.4 V at 10 mA g^{-1}. $Na_{4/7}[\square_{1/7}Ti_{1/7}Mn_{5/7}]O_2$ exhibits excellent cycling performance, showing no capacity loss. Whereas, $Na_{4/7}[\square_{1/7}Mn_{6/7}]O_2$ only retains 82% of its initial discharge capacity. The aforementioned tests show that Ti^{4+} has a remarkable effect on the cycling stability, especially for the oxygen redox reversibility. In order to study the role of Ti^{4+} in improving the reversibility of the insertion and extraction of Na^+ ions in $Na_{4/7}[\square_{1/7}Ti_{1/7}Mn_{5/7}]O_2$ a computational study was performed (see Section 2.4). The rate capability of $Na_{4/7}[\square_{1/7}Mn_{6/7}]O_2$ and $Na_{4/7}[\square_{1/7}Ti_{1/7}Mn_{5/7}]O_2$ cycled between 3.0 and 4.4 V at 50, 100, 200 mA g^{-1} has also been tested. Fig. 3(d) reveals that both materials exhibit similar rate performance in this voltage window.

2.2. Structural evolution and charge compensation mechanism

The changes in structure of $Na_{4/7}[\square_{1/7}Ti_{1/7}Mn_{5/7}]O_2$ upon Na^+ ion extraction and insertion were investigated using powder X-ray diffraction (PXRD). *Ex situ* PXRD patterns were collected over the initial charge/discharge cycle between 1.6 and 4.4 V

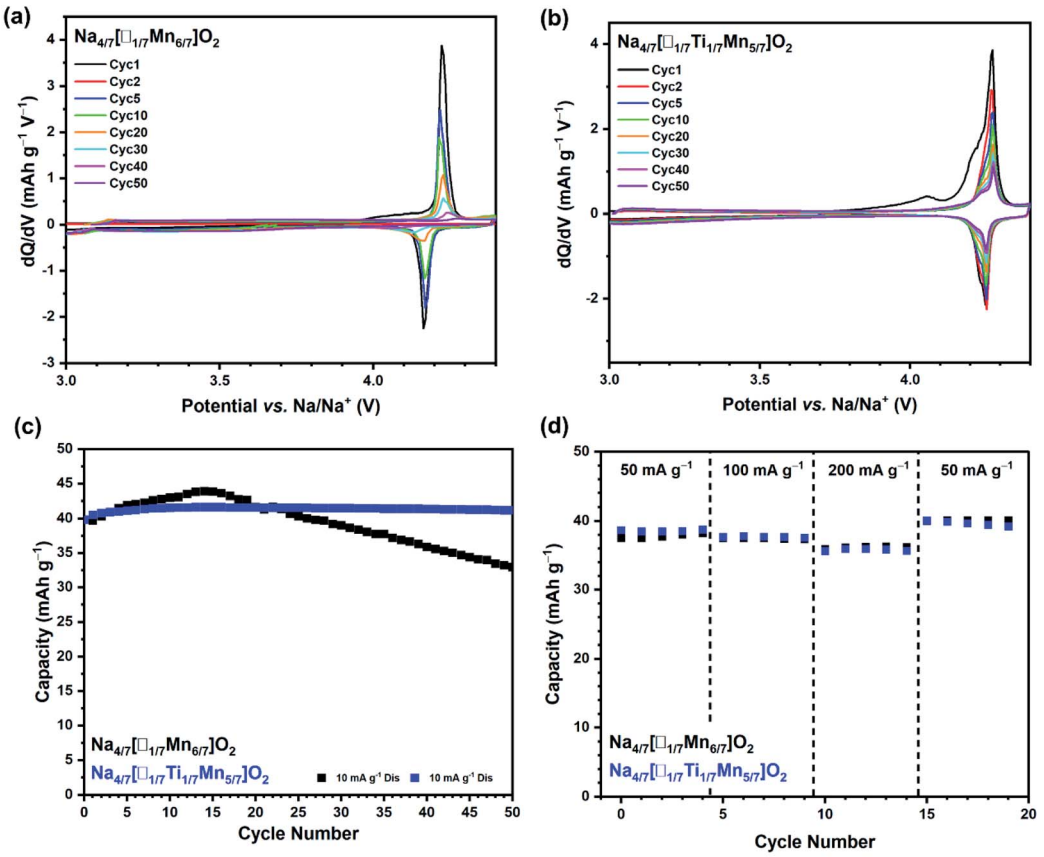

Fig. 3 Derivative dQ/dV plots of (a) $Na_{4/7}[\square_{1/7}Mn_{6/7}]O_2$ and (b) $Na_{4/7}[\square_{1/7}Ti_{1/7}Mn_{5/7}]O_2$, collected at 30 °C between 3.0 and 4.4 V at a rate of 10 mA g^{-1} showing the first (black), second (red), fifth (blue), tenth (green), twentieth (orange), thirtieth (cyan), fortieth (pink) and fiftieth (purple) cycles. (c) Galvanostatic cycling performance of $Na_{4/7}[\square_{1/7}Mn_{6/7}]O_2$ (black) and $Na_{4/7}[\square_{1/7}Ti_{1/7}Mn_{5/7}]O_2$ (blue) cycled between 3.0 and 4.4 V at a current rate of 10 mA g^{-1} at 30 °C, showing the discharge capacities. (d) Rate capability of $Na_{4/7}[\square_{1/7}Mn_{6/7}]O_2$ (black) and $Na_{4/7}[\square_{1/7}Ti_{1/7}Mn_{5/7}]O_2$ (blue) cycled between 3.0 and 4.4 V at a current rate of 50, 100, and 200 mA g^{-1} at 30 °C, showing the discharge capacities.

(Fig. 4(a)). Rietveld refinements were performed, and the fits obtained for data from the electrodes charged to 4.4 V (CH4.4V), and then subsequently discharged to 3.0 V (DIS3.0V) and 1.6 V (CYC1.6V) are shown in Fig. 4(b)–(d), respectively. The PXRD pattern for $Na_{4/7}[\square_{1/7}Ti_{1/7}Mn_{5/7}]O_2$ after charge to 4.4 V (Fig. 4(b)), can be fitted to a simple P3-type model with the $R3m$ space group, with refined unit cell parameters a = 2.849(1), c = 16.637(14) Å. This shows that upon Na^+ ion removal there is an increase in the crystallographic symmetry, with a transition from the $Na_{4/7}[\square_{1/7}Mn_{6/7}]O_2$ structure ($P\bar{1}$ space group) for pristine $Na_{4/7}[\square_{1/7}Ti_{1/7}Mn_{5/7}]O_2$ (Fig. 1(a)) to a structure which can be well-described in $R3m$ symmetry, demonstrating that the P3 oxygen stacking sequence is preserved (Table S5†), consistent with the structural evolution observed for $Na_{4/7}[\square_{1/7}Mn_{6/7}]O_2$.[22,29] Furthermore, $Na_{4/7}[\square_{1/7}Ti_{1/7}Mn_{5/7}]O_2$ shows a minimal volume contraction of ~0.6%. Upon subsequent Na^+ ion insertion, the PXRD pattern after discharge to 3.0 V can effectively be modelled using the $P\bar{1}$ space group (Fig. 4(c)), showing that the $Na_{4/7}[\square_{1/7}Mn_{6/7}]O_2$ structure is restored and reveals a small volume contraction of ~0.3% relative to the pristine phase. Moreover, upon charge to 4.4 V and subsequent discharge to 3.0 V, the shift in the position of the 001 diffraction peak (7.39° 2θ), corresponding to the interlayer distance between the $[\square_{1/7}Ti_{1/7}Mn_{5/7}]O_2$ layers is negligible (0.01° 2θ), suggesting that the interlayer distance is preserved at 5.57 Å which agrees with data reported for $Na_{4/7}[\square_{1/7}Mn_{6/7}]O_2$.[21,23] Additionally, the superstructure is restored on discharge and it is likely that the superstructure is preserved after charge to 4.4 V, but cannot be resolved in *ex situ* measurements. Upon further Na^+ ion insertion, the PXRD pattern of $Na_{4/7}[\square_{1/7}Ti_{1/7}Mn_{5/7}]O_2$ discharged to 1.6 V after charge to 4.4 V (Fig. 4(d)), shows partial transformation of 15% to an O3-type phase which shows an expansion of 1.5% relative to the volume of the pristine phase. This is reasonable since the insertion of additional Na^+ ions increases the coulombic repulsion between the Na and Mn cations and the P3 structure undergoes a structural transformation to the O3-type phase to relieve this repulsion.[30,42] Since 85% of the $Na_{4/7}[\square_{1/7}Mn_{6/7}]O_2$ structure is retained and shows essentially no volume change, there is an average overall expansion of ~0.2% relative to the pristine phase. $Na_{4/7}[\square_{1/7}Ti_{1/7}Mn_{5/7}]O_2$ undergoes minimal volume changes upon cycling, agreeing with *in situ* PXRD measurements previously reported by Liu *et al.* who also showed a larger volume change of 6.8% for

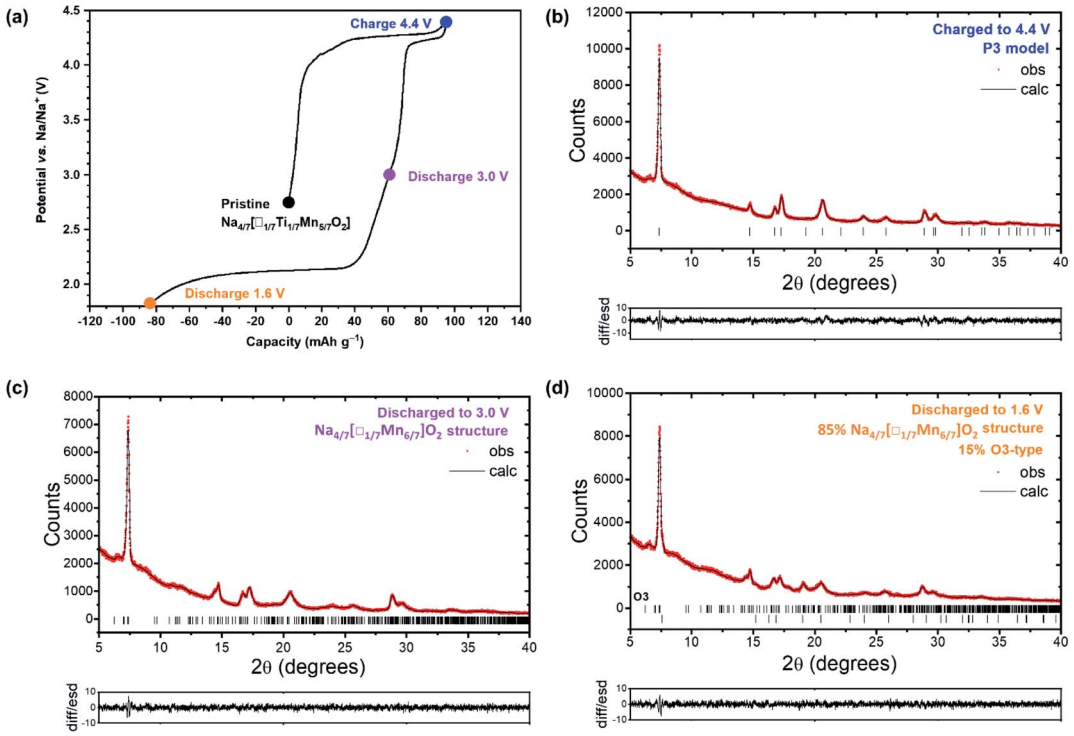

Fig. 4 (a) Galvanostatic charge/discharge profile for $Na_{4/7}[\square_{1/7}Ti_{1/7}Mn_{5/7}]O_2$ cycled at 30 °C between 1.6 and 4.4 V at a rate of 10 mA g^{-1}, showing the voltages for the *ex situ* PXRD measurements. (b) Laboratory X-ray Rietveld fits for $Na_{4/7}[\square_{1/7}Ti_{1/7}Mn_{5/7}]O_2$ charged to 4.4 V, (c) cycled between 3.0 and 4.4 V, and (d) cycled between 1.6 and 4.4 V. The observed data points are shown in red, with the fitted profiles in black. Tick marks indicate allowed reflections.

$Na_{4/7}[\square_{1/7}Mn_{6/7}]O_2$,[29] correlating enhanced structural stability with superior cycle life.

To follow changes in the oxidation states of Mn, Ti and O during the first cycle, *ex situ* SXAS spectra were collected at different states of charge and discharge over the first cycle between 3.0 and 4.4 V. SXAS measurements were collected at the Mn $L_{2,3}$-edge (Fig. 5(a)), Ti $L_{2,3}$-edge (Fig. 5(b)) and O K-edge (Fig. S7(a)†) using the partial fluorescence yield (PFY) and total electron yield (TEY) modes. During cycling the Mn $L_{2,3}$-edge spectrum of pristine $Na_{4/7}[\square_{1/7}Ti_{1/7}Mn_{5/7}]O_2$ shows absorption peaks at 643.4 and 653.4 eV, which correspond to the L_3 and L_2 edges, respectively, and is consistent with Mn^{4+}.[43] The spectra show no shift in energy upon cycling (Fig. 5(c)), indicating that Mn remains tetravalent and does not participate in the charge transfer mechanism between 3.0 and 4.4 V. The Ti $L_{2,3}$-edge SXAS spectrum of the pristine electrode shows that Ti exists as Ti^{4+} and similarly reveals no changes upon charge/discharge (Fig. 5(c)), confirming that Ti does not contribute towards the capacity between 3.0 and 4.4 V.[44] Therefore, these data suggest that lattice oxygen participates in the charge compensation mechanism.

The O K-edge SXAS spectrum of pristine $Na_{4/7}[\square_{1/7}Ti_{1/7}Mn_{5/7}]O_2$ shows two pre-edge peaks which correspond to the excitation from the O 1s to unoccupied O 2p states hybridised with the transition metal 3d t_{2g} (*ca.* 530 eV) and e_g states (532 eV).[12,45,46] The broad peaks above 535 eV are characteristic of transitions to the O 2p states hybridised with transition metal 4s and 4p states. The area under the pre-edge peak (between 525 and 533 eV) relates to changes in the density of empty states above the Fermi level. The relative intensity of the pre-edge peaks is shown in Fig. S7(b).† This reveals minimal intensity changes and does not provide sufficient evidence of oxygen redox activity. These metastable O^{n-} species where $3 \geq n \geq 1$ relax over time and it is reasonable to assume that they relaxed prior to data acquisition. Therefore, electron paramagnetic resonance (EPR) spectroscopy (Fig. 6) and Raman spectroscopy (Fig. S10†) were used to investigate the oxygen redox activity. By contrast EPR spectroscopy demonstrate stronger indications of oxygen anion redox activity, consistent with the Mn and Ti L-edge SXAS spectra (Fig. 5), and these findings are discussed in more detail below.

Ex situ EPR measurements were collected for $Na_{4/7}[\square_{1/7}Mn_{6/7}]O_2$ and $Na_{4/7}[\square_{1/7}Ti_{1/7}Mn_{5/7}]O_2$ at different states of charge and discharge over the first cycle between 3.0 and 4.4 V. EPR spectroscopy can identify the formation and disappearance of radical oxygen species and therefore, provide mechanistic insights into oxygen anion redox.[8,47,48] Fig. 6 presents the evolution of the EPR spectra for $Na_{4/7}[\square_{1/7}Ti_{1/7}Mn_{5/7}]O_2$ at various states of charge and discharge. Pristine $Na_{4/7}[\square_{1/7}Ti_{1/7}Mn_{5/7}]O_2$, without conductive carbon additive, shows an intense broad symmetric signal, attributed to the antiferromagnetic Mn^{4+}–O. The Mn^{4+}–O EPR signal presents a single Lorentzian line shape centred at $g \approx 2.00$.[49] The addition of conductive carbon C65 to $Na_{4/7}[\square_{1/7}Ti_{1/7}Mn_{5/7}]O_2$ gives rise to a sharp peak, as shown for the $Na_{4/7}[\square_{1/7}Ti_{1/7}Mn_{5/7}]O_2$ electrodes, due to

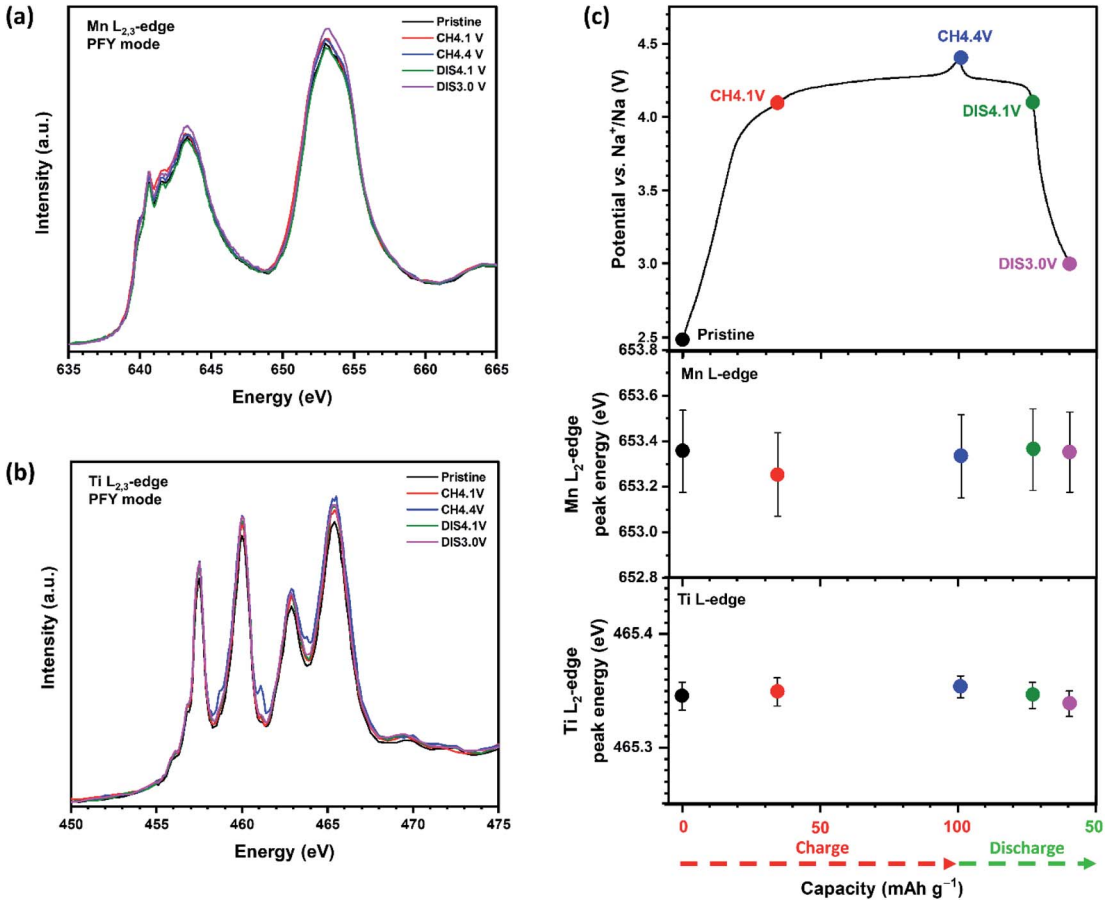

Fig. 5 Electronic structure changes of $Na_{4/7}[\square_{1/7}Ti_{1/7}Mn_{5/7}]O_2$ during charge and discharge. (a) *Ex situ* soft X-ray absorption spectra for Mn $L_{2,3}$-edge in partial fluorescence yield mode (PFY). (b) *Ex situ* soft X-ray absorption spectra for Ti $L_{2,3}$-edge in PFY. (c) First-cycle charge–discharge load curve and the points indicate the states of charge and discharge at which *ex situ* measurements were collected. Variations in the Mn L_2-peak energy and Ti L_2 e_g peak energies.

delocalised electrons within C65. After charge to 4.1 V, the intensity of the EPR spectrum decreases relative to that of pristine $Na_{4/7}[\square_{1/7}Ti_{1/7}Mn_{5/7}]O_2$. Upon further charge to 4.4 V, the intensity of the EPR signal reduces further. Based on the SXAS data (Fig. 5), Mn and Ti do not participate in the charge compensation mechanism between 3.0 and 4.4 V. Therefore, the extraction of Na^+ ions upon charge to 4.4 V is associated with O^{2-} oxidation to O_2^{n-} where $3 \geq n \geq 1$. Of these anion redox species, only O_2^{3-} and superoxo O_2^- species have a single unpaired electron ($S = \frac{1}{2}$) and are therefore detectable by EPR. Whereas peroxo O_2^{2-} has an even number of paired electrons ($S = 0$) and is EPR-silent. Upon discharge, the EPR signal intensity increases with decreasing potential, demonstrating the reversibility of the O_2^{n-} redox reaction.

As for $Na_{4/7}[\square_{1/7}Mn_{6/7}]O_2$, Fig. S8† shows the EPR spectra for $Na_{4/7}[\square_{1/7}Mn_{6/7}]O_2$ cycled between 3.0 and 4.4 V. $Na_{4/7}[\square_{1/7}Mn_{6/7}]O_2$ presents the same trend as $Na_{4/7}[\square_{1/7}Ti_{1/7}Mn_{5/7}]O_2$ upon charge/discharge. The intensity of the EPR signal similarly decreases on charge to 4.4 V and increases again on discharge. These data also agree well with EPR data previously reported for $Na_{4/7}[\square_{1/7}Mn_{6/7}]O_2$ by Song *et al.*[22]

Further analysis of the same samples after 5 days (Fig. S9†) shows a change in the EPR signals of the electrodes after charge to 4.4 V. The $Na_{4/7}[\square_{1/7}Mn_{6/7}]O_2$ electrode after charge to 4.4 V reveals an increase in intensity after 5 days, suggesting that the O_2^{n-} species formed at the end of charge is unstable and relaxes over 5 days. The $Na_{4/7}[\square_{1/7}Ti_{1/7}Mn_{5/7}]O_2$ system shows a similar relaxation of the EPR signal after five days but to a lesser extent to that of the $Na_{4/7}[\square_{1/7}Mn_{6/7}]O_2$ system. Thereby, implying that the presence of Ti^{4+} increases the stability of the O_2^{n-} species somewhat. Based on these data, the O_2^{n-} species decays within days of being charge/discharged and therefore explains the minimal changes observed for the SXAS O K-edge spectra (Fig. S7†), as these data were collected roughly four weeks after preparation.

Raman spectroscopy was used to evaluate the structural evolution of $Na_{4/7}[\square_{1/7}Ti_{1/7}Mn_{5/7}]O_2$ upon cycling and examine if peroxide species, O_2^{2-}, form. Pristine $Na_{4/7}[\square_{1/7}Ti_{1/7}Mn_{5/7}]O_2$ and $Na_{4/7}[\square_{1/7}Ti_{1/7}Mn_{5/7}]O_2$ mixed with carbon C65 (Fig. S10(a)†) show an intense band at ~640 cm^{-1} and a broad shoulder at ~582 cm^{-1} which probably correspond to the O–TM–O bending and TM–O stretching modes (TM = Mn, Ti) of the transition metal TMO_6 layer, respectively. Li *et al.* examined

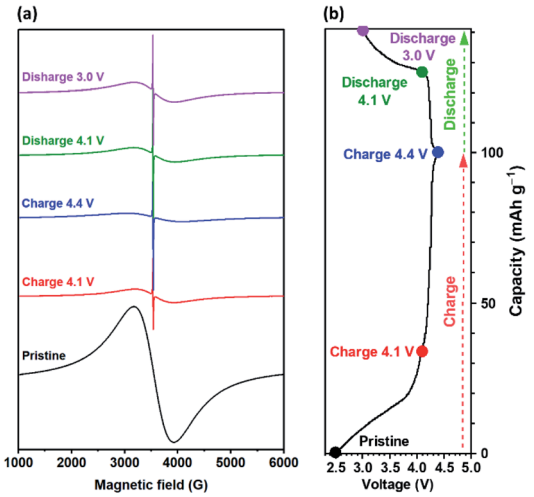

Fig. 6 (a) EPR spectra of pristine $Na_{4/7}[\square_{1/7}Ti_{1/7}Mn_{5/7}]O_2$ and *ex situ* electrodes of $Na_{4/7}[\square_{1/7}Ti_{1/7}Mn_{5/7}]O_2$ cycled between 3.0 and 4.4 V at 10 mA g^{-1}, mixed with conductive carbon C65 additive. EPR spectra were collected on the same day after cycling ceased and normalised based on the mass of the sample. The sharp, intense peak is assigned to conductive carbon C65 additive. (b) The corresponding galvanostatic charge/discharge profile with the voltages highlighted where the *ex situ* EPR measurements were conducted.

the structural evolution of $Na_{4/7}[\square_{1/7}Mn_{5/7}]O_2$ upon cycling and likewise observed bands at 638 and 580 cm^{-1} for the pristine material.[23] Fig. S10(b)† presents the *ex situ* Raman spectra recorded for $Na_{4/7}[\square_{1/7}Ti_{1/7}Mn_{5/7}]O_2$ at different states of charge and discharge over the first cycle between 3.0 and 4.4 V. These spectra show that the position of the TM–O (TM = Mn, Ti) bands remain constant upon cycling which agrees with the PXRD results (Fig. 4, *i.e.*, no structural transformation between 3.0 and 4.4 V) and Raman data previously presented for $Na_{4/7}[\square_{1/7}Mn_{5/7}]O_2$.[23] Essentially the spectra do not reveal any clear additional bands or changes in intensity in the region where O–O stretches (700–900 cm^{-1}) have been observed for peroxide-containing species (*e.g.*, Li_2O_2, Na_2O_2, H_2O_2 and ZnO_2).[12] Unfortunately, contributions from the EL-Cell holder/separator (~790–1090 cm^{-1}) are within the same region for O–O stretches and therefore hinder definitive detection of O–O bonds. This can be seen in Fig. S10(a),† where the bands within the ~790–1090 cm^{-1} region are only observed for the measurements carried out inside the EL-Cell for both the pristine $Na_{4/7}[\square_{1/7}Ti_{1/7}Mn_{5/7}]O_2$ and $Na_{4/7}[\square_{1/7}Ti_{1/7}Mn_{5/7}]O_2$ mixed with carbon C65. Similar to this work, *ex situ* Raman spectroscopic studies performed on $Na_{4/7}[\square_{1/7}Mn_{6/7}]O_2$ could not confirm the presence of peroxide species O_2^{2-} upon charging.[23] However, *in situ* Raman spectroscopic experiments on related systems have revealed bands between 700 and 900 cm^{-1}, corresponding to O–O stretches of peroxo-species.[50–52]

2.3. Interpretation on the increased voltages after Ti substitution

To gain insight into the origin of the higher potentials observed for $Na_{4/7}[\square_{1/7}Ti_{1/7}Mn_{5/7}]O_2$ (Fig. 2), theoretical voltage profiles were constructed, and the associated electronic structures were analysed. We first constructed model atomic structures for $Na_x[\square_{1/7}Mn_{6/7}]O_2$ and $Na_x[\square_{1/7}Ti_{1/7}Mn_{5/7}]O_2$, with Na content being $0.0 \le x \le 6/7$, based on the x values (~0.25 to 1.0 Na) from the galvanostatic charge/discharge curves over the voltage range 1.6–4.4 V (see Fig. 2). In this regard, partially desodiated phases with $x < 4/7$ were generated by removing Na^+ ions from primitive $Na_{4/7}[\square_{1/7}Mn_{6/7}]O_2$ and $Na_{4/7}[\square_{1/7}Ti_{1/7}Mn_{5/7}]O_2$, whereas phases after discharging with $x > 4/7$ were created by adding Na^+ ions into stable interstitial sites (see ESI† for more details). Tables S6 and S7† show the constructed ground state structures of fully discharged $Na_{6/7}[\square_{1/7}Mn_{6/7}]O_2$ and $Na_{6/7}[\square_{1/7}Ti_{1/7}Mn_{5/7}]O_2$.

After generating intermediate $Na_x[\square_{1/7}Mn_{6/7}]O_2$ and $Na_x[\square_{1/7}Ti_{1/7}Mn_{5/7}]O_2$ phases, with Na contents being $0.0 \le x \le 6/7$, we next searched the stable low-energy structures that primarily determine the shape of theoretical voltage curves. This was attained by calculating total energies of all symmetry unique atomic arrangements, followed by plotting their convex-hull diagrams as a function of Na content (Fig. 7(a)). For both $Na_x[\square_{1/7}Mn_{6/7}]O_2$ and $Na_x[\square_{1/7}Ti_{1/7}Mn_{5/7}]O_2$, the convex-hull diagrams show that there are six stable structures, with Na concentrations of $x = 1/7$, 2/7, 3/7, 4/7 and 6/7. This suggests that voltage profiles upon charging from $x = 4/7$ to 2/7 are characterised by two voltage plateaux, whereas those upon discharge from $x = 4/7$ to 6/7 will have a single voltage plateau.

Close comparison of the formation energies of two convex-hull diagrams of $Na_x[\square_{1/7}Mn_{6/7}]O_2$ and $Na_x[\square_{1/7}Ti_{1/7}Mn_{5/7}]O_2$ show that, upon charging, Ti-doped materials are relatively unstable, as can be confirmed by the higher formation energy of $Na_{2/7}[\square_{1/7}Ti_{1/7}Mn_{5/7}]O_2$ than $Na_{2/7}[\square_{1/7}Mn_{6/7}]O_2$ (see inset of Fig. 7(a)). This suggests that the addition of Ti destabilises the desodiated materials, resulting in the increase of charging voltage. By incorporating the stable phases predicted from the convex-hull diagrams and other unstable Na arrangements that can form under thermal vibration at room temperature, we calculated theoretical voltage profiles of $Na_x[\square_{1/7}Mn_{6/7}]O_2$ and $Na_x[\square_{1/7}Ti_{1/7}Mn_{5/7}]O_2$ (Fig. 7(b) and (c)). In this calculation, the mean and standard deviations of voltages that arise from differing Na arrangements are considered to reflect the potential errors that occur during Na diffusion (see ESI†). The predicted voltage profiles are in good agreement with experimental data, especially for the Ti-substituted material which shows slightly higher voltages over $Na_{4/7}[\square_{1/7}Mn_{6/7}]O_2$. The voltages required to remove and insert Na from Ti-substituted $Na_x[\square_{1/7}Ti_{1/7}Mn_{5/7}]O_2$ are greater by 0.08–0.15 V and 0.09 V, respectively, which is consistent with the capacity *versus* voltage and dQ/dV plots shown in Fig. 2.

Having reproduced the higher voltages of Ti-substituted $Na_{4/7}[\square_{1/7}Mn_{6/7}]O_2$ (Fig. 7), we proceeded to analyse the redox mechanisms of voltage plateaux to identify the origin of the increased voltages. To this end, projected densities of states were calculated for differing Na concentrations (x) of $Na_x[\square_{1/7}Mn_{6/7}]O_2$ and $Na_x[\square_{1/7}Ti_{1/7}Mn_{5/7}]O_2$ (Fig. 9). For both materials, Na extraction during charging oxidises non-bonding oxygens adjacent to the unoccupied Mn sites, causing the oxygens to have localised excess holes. On the other hand, adding excess Na into

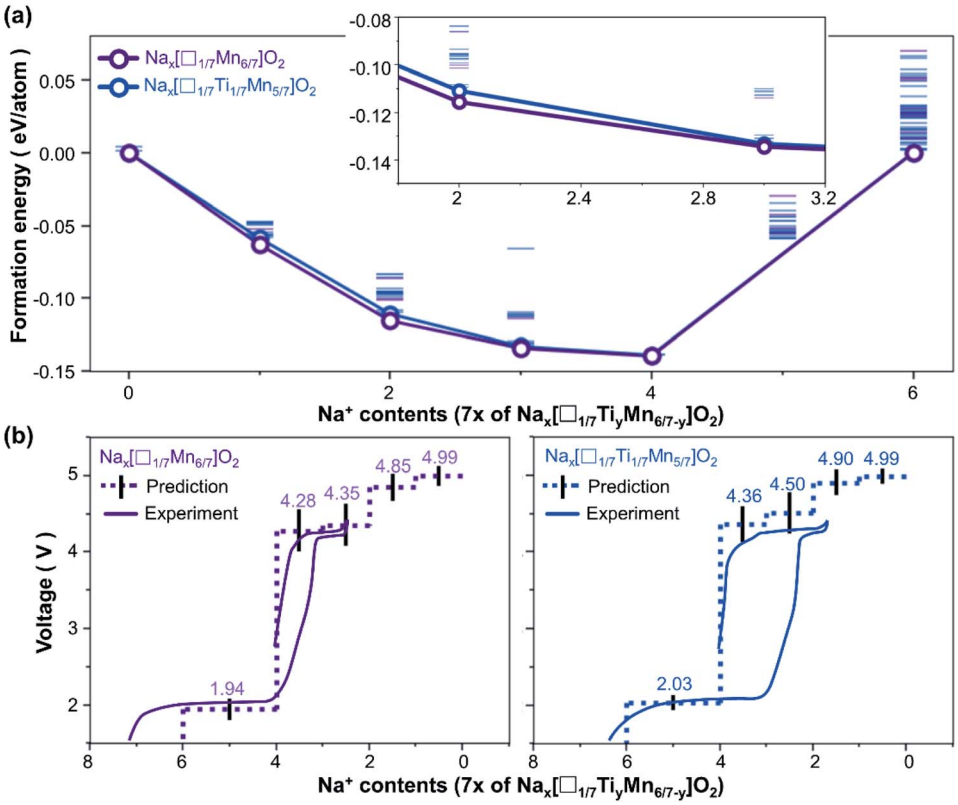

Fig. 7 (a) Calculated formation energies of all intermediate phases constructed from $Na_x[\square_{1/7}Mn_{6/7}]O_2$ and $Na_x[\square_{1/7}Ti_{1/7}Mn_{5/7}]O_2$. Convex hull diagrams were plotted by connecting ground state structures (empty circles). Unstable atomic configurations are denoted as horizontal lines for reference. (b) Theoretical and experimental voltage curves of $Na_x[\square_{1/7}Mn_{6/7}]O_2$ and $Na_x[\square_{1/7}Ti_{1/7}Mn_{5/7}]O_2$. Among all symmetrically unique Na and Ti arrangements, those that can form under thermal vibration energy (0.0259 eV) at room temperature are considered. Mean and standard deviation of voltages calculated from the selected atomic arrangements are denoted as dotted and vertical black lines, respectively. Mean theoretical voltages are denoted above each plateau for better visualisation.

$Na_{4/7}[\square_{1/7}Mn_{6/7}]O_2$ and $Na_{4/7}[\square_{1/7}Ti_{1/7}Mn_{5/7}]O_2$ accompanies the localisation of excess electrons on Mn^{4+}, reducing it to Mn^{3+}. The above results indicate that the high potentials (4.3 V) during charging ($x < 4/7$) arise from anion redox, as revealed by EPR measurements (Fig. 6), whereas the low potentials (2.0 V) during discharging ($4/7 < x < 6/7$) are associated with the Mn^{3+}/Mn^{4+} redox couple. Unlike Mn and O, Ti does not participate in the redox reaction (between 1.6 and 4.4 V), as none of the excess electrons/holes are centred near Ti upon charge or discharge.

Despite Ti being redox-inactive upon cycling, it influences the bond ionicity and associated electronic structures. Ti, with slightly lower electronegativity than Mn, tends to make stronger ionic Ti–O bonds, as revealed by the greater band gap of $Na_{4/7}[\square_{1/7}Ti_{1/7}Mn_{5/7}]O_2$ compared to that of $Na_{4/7}[\square_{1/7}Mn_{6/7}]O_2$. From an atomistic perspective, Ti makes adjacent O 2p orbitals more stable and therefore, harder to remove. Upon Na extraction, this causes the electron holes to be localised away from Ti, as shown by the partial charge density of $Na_{2/7}[\square_{1/7}Ti_{1/7}Mn_{5/7}]O_2$ in Fig. 8(b). Additional calculations of the local Madelung potentials (Fig. S11†),[53,54] further support this argument, that oxygens positioned further away from Ti atoms have lower Madelung potential and can readily be oxidised upon charging. Such hindrance of Ti on anion redox increases the energy required to remove Na, resulting in greater charge voltages.

The stronger ionicity of Ti–O bonds also contributes to the increase in the discharge voltage: when a less electronegative Ti atom bonds with an oxygen, the oxygen has a greater share of electrons, thereby making the nearby Mn–O bonding more ionic (Fig. S12†). The increased ionicity of Mn–O bonds reduces the repulsion between the bonding and antibonding orbitals, pulling the antibonding orbitals away from the Na^+/Na redox couple.[55] These changes are observed as higher discharge voltages for $Na_{4/7}[\square_{1/7}Mn_{6/7}]O_2$ and $Na_{4/7}[\square_{1/7}Ti_{1/7}Mn_{5/7}]O_2$, as their discharge voltages are related to the location of the antibonding Mn–O hybrid orbitals with respect to the Na^+/Na redox couple.

2.4. Interpretation of enhanced cyclability after Ti substitution

The cation and anion redox couples have their own respective mechanisms that can reduce the cycling stability of Mn-based materials. Cation redox reactions can cause Jahn–Teller distortion of MnO_6 octahedra upon reduction of Mn^{4+} to Mn^{3+}, reducing the structural stability of Mn-based materials.[56] To better understand the effect of Ti-substitution on the structural stability and associated cyclability of $Na_{4/7}[\square_{1/7}Mn_{6/7}]O_2$ upon cation redox, we compared the structural changes upon cycling before and after Ti-substitution (Fig. 9). The volumes of the MnO_6

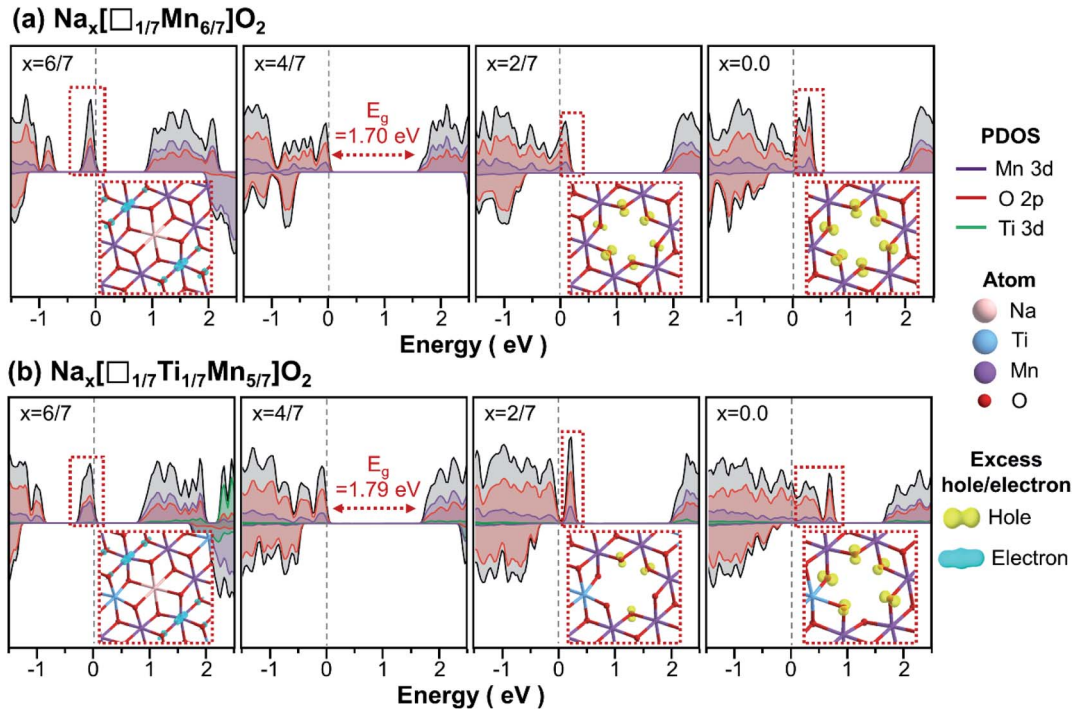

Fig. 8 Projected density of states of primitive (a) $Na_x[\square_{1/7}Mn_{6/7}]O_2$ and (b) $Na_x[\square_{1/7}Ti_{1/7}Mn_{5/7}]O_2$ calculated from the most stable atomic arrangement at each Na composition of $x = 6/7$, 4/7, 2/7, and 0.0. The insets show the partial charge densities of excess holes (electrons) created after desodiation (sodiation) of $Na_{4/7}[\square_{1/7}Mn_{6/7}]O_2$ or $Na_{4/7}[\square_{1/7}Ti_{1/7}Mn_{5/7}]O_2$.

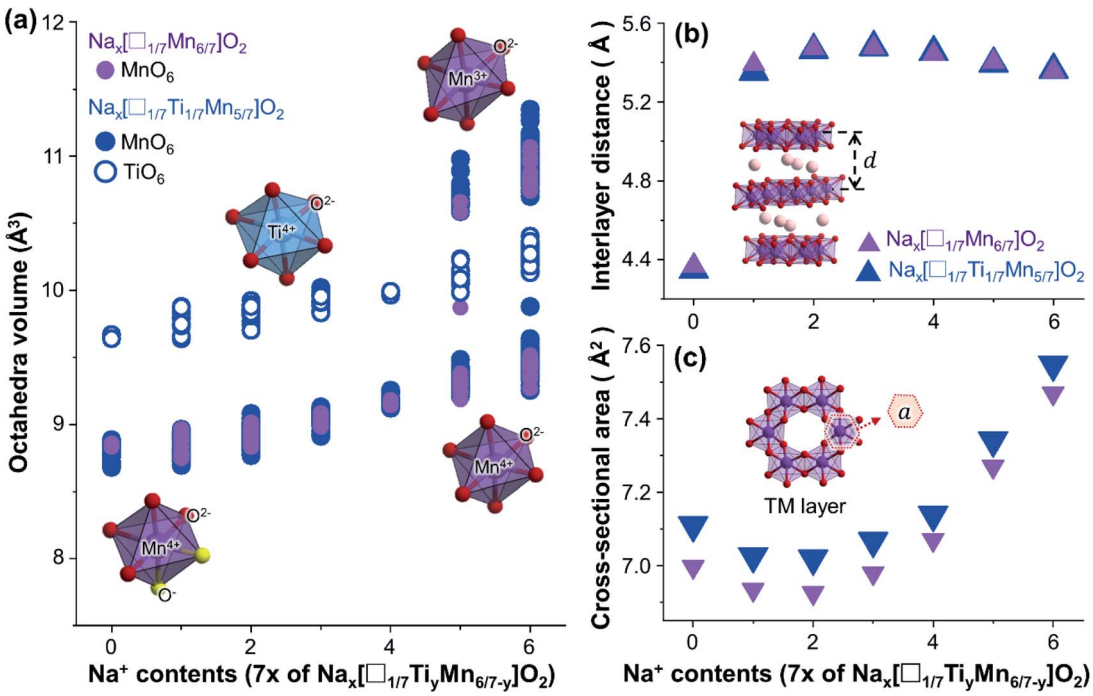

Fig. 9 (a) Volumes of MnO_6 and TiO_6 octahedra of all $Na_x[\square_{1/7}Mn_{6/7}]O_2$ and $Na_x[\square_{1/7}Ti_{1/7}Mn_{5/7}]O_2$ structures optimised in this study. Representative oxidation states of octahedra at each Na composition are represented in the insets. Changes in the (b) average interlayer distance (d) and (c) average cross-sectional area (a) of TMO_6 octahedra calculated for $Na_x[\square_{1/7}Mn_{6/7}]O_2$ and $Na_x[\square_{1/7}Ti_{1/7}Mn_{5/7}]O_2$ structures, plotted with respect to their Na contents.

octahedra for $Na_{4/7}[\square_{1/7}Mn_{6/7}]O_2$ and $Na_{4/7}[\square_{1/7}Ti_{1/7}Mn_{5/7}]O_2$ (Fig. 9(a)), tend to expand with increasing Na content. The greatest volumetric changes occur during discharge from $x = 4/7$ to 6/7, where MnO_6 octahedra volumes are enlarged by up to roughly 20%. Such large volumetric change can be attributed to excess electrons supplied from inserted Na^+ ions, which reduces Mn^{4+} to Mn^{3+} and form Jahn–Teller distorted $Mn^{3+}O_6$ octahedra, with larger volumes. On the other hand, the charging process from $x = 4/7$ to 0.0 is governed by anion redox reactions and compresses the octahedra by oxidation of O^{2-} to O^- with smaller ionic radius. Compared to the volume changes from the cation redox couples, the volume changes from this anion redox reaction have a minor effect, which can enlarge/compress octahedra volumes by up to only ~5%. Therefore, between 1.6 and 4.4 V, where both cation and anion redox reactions occur, the major structural degradation arises from cation redox reactions. From this perspective, one can improve the structural stability of positive electrodes by reducing the voltage window above cation redox voltage of ~2.1 V. However, this method compromises cation-redox capacities, as revealed by the galvanostatic cycling performance in Fig. 2.

Another important finding from Fig. 9(a) is that the volumes of TiO_6 octahedra are located in between those of $Mn^{3+}O_6$ and $Mn^{4+}O_6$ during cation redox reactions (see Na contents range of $4/7 < x < 6/7$). This is because of the ionic radius of Ti^{4+} (0.605 Å), is close to the average value of those of Mn^{3+} (0.645 Å) and Mn^{4+} (0.53 Å).[33] Moreover, unlike MnO_6 octahedra, these TiO_6 octahedra do not undergo cation redox reactions and are immune to the associated volumetric changes. This suggests that TiO_6 octahedra are mechanically stable and act as a buffer that mediates the structural changes of MnO_6 octahedra upon cation redox reactions. In this regard, Ti-substitution can be an effective method to relieve the structural degradation and improve cyclability under the wide voltage windows, while exploiting the large capacities from Mn^{3+}/Mn^{4+} redox couples.

Owing to the larger ionic radius of Ti^{4+} compared to Mn^{4+}, the addition of Ti increases the size of the TMO_2 layer and thereby the size of the unit cell. Fig. 9(b) and (c) shows the effect of Ti on the interlayer distance (d) and the area of octahedra cross-sectioned by a plane parallel to TMO_2 layer. The interlayer distance is slightly greater for $Na_{4/7}[\square_{1/7}Ti_{1/7}Mn_{5/7}]O_2$ (5.45 Å) than $Na_{4/7}[\square_{1/7}Mn_{6/7}]O_2$ (5.44 Å), which is consistent with (001) diffraction peaks from PXRD results. However, the broadened interlayer spacing may not persist upon cycling, as the interlayer spacing becomes greater for $Na_{4/7}[\square_{1/7}Mn_{6/7}]O_2$ for Na composition ranges (x = 0.0, 1/7, 2/7, and 5/7). Unlike the interlayer spacing, the cross-sectional area of TMO_6 octahedra is greater for the Ti-substituted material over the full range of Na compositions (Fig. 9(c)).

The above results suggest that Ti-substitution in $Na_{4/7}[\square_{1/7}Mn_{6/7}]O_2$ primarily enlarges the TMO_2 layer parallel to the (001) planes, while having only minor influences on the interlayer spacing. In practical experiments, such structural changes may cause negative effects on the rate performances of the positive electrode materials, as they will lengthen the pathways for Na diffusion along (001) planes. Further examination of Fig. 9(b) and (c) shows that, upon discharge from $x = 2/7$ to 6/7, both materials show decrease in their interlayer distances, accompanied by a widening of the cross-sectional area. These structural changes can be explained based on the type of Na sites: when examining the calculated (see ESI†) and observed structures (see Rietveld refinement results in Table S1†) of $Na_x[\square_{1/7}Mn_{6/7}]O_2$ and $Na_x[\square_{1/7}Ti_{1/7}Mn_{5/7}]O_2$, Na atoms prefer to be in prismatic sites under Na-poor conditions ($x = 2/6$) and gradually transform to octahedral sites as the Na content increases to $x = 6/7$, as confirmed by *ex situ* PXRD results (Fig. 4). This is common for transition metal oxides, as prismatic and octahedral stackings are the optimal configurations to minimise face-sharing between cations and the associated electrostatic repulsions under Na-poor and Na-rich conditions, respectively.[57,58] Among these two stackings, prismatic sites are characterised by greater interlayer distance and smaller cross-sectional TM layer area compared to octahedra,[57,59] resulting in wider and shorter Na diffusion channels for prismatic stackings. Both $Na_x[\square_{1/7}Mn_{6/7}]O_2$ and $Na_x[\square_{1/7}Ti_{1/7}Mn_{5/7}]O_2$ undergo transition from prismatic to octahedral stacking, which can cause the cyclability to deteriorate.

3. Conclusions

Partial substitution of Mn by Ti has been shown to enhance the electrochemical performance of $Na_{4/7}[\square_{1/7}Mn_{6/7}]O_2$. Ti-substituted $Na_{4/7}[\square_{1/7}Ti_{1/7}Mn_{5/7}]O_2$ delivers a highly reversible capacity of 146 mA h g^{-1} after 50 cycles with 77% capacity retention within the voltage range 1.6–4.4 V at 10 mA g^{-1}. In the voltage range of 3.0–4.4 V, $Na_{4/7}[\square_{1/7}Ti_{1/7}Mn_{5/7}]O_2$ shows no capacity fade after 50 cycles, based on oxygen redox reactions. The improved cyclability is likely to be rooted in the presence of TiO_6 octahedra that maintain their volume upon cycling, thus relieving structural distortions arising from Jahn–Teller distorted $Mn^{3+}O_6$ octahedra below 3.0 V. The stable anion redox activity above 3.0 V, on the other hand, is believed to arise from the low electronegativity of Ti that enhances bond ionicity and thereby bond strength of Mn–O bonds. The low electronegativity of Ti also stabilises the adjacent O 2p orbitals, increasing the charge/discharge voltages of $Na_{4/7}[\square_{1/7}Ti_{1/7}Mn_{5/7}]O_2$. Finally, despite the larger ionic radius of the Ti^{4+}, its effect on the interlayer separation is insignificant, as the so-formed TiO_6 octahedra distort the TMO_2 layer to be stretched mostly along the TM layer direction, as the TiO_6 octahedra distort rather than widening interlayer distances. This work provides new methods to preserve the structural integrity in oxygen redox active sodium layered oxides which can achieve high energy densities and show enhanced oxygen redox reversibility.

Author contributions

The manuscript was written through contributions of all authors. All authors have given approval to the final version of the manuscript.

Conflicts of interest

There are no conflicts to declare.

Acknowledgements

The authors are grateful for the provision of beam time and assistance from instrument scientists at beamline I11 at Diamond (Rapid Access experiment CY26699). We gratefully acknowledge Spring 8 for beamtime (Proposal No. 2021A1425) and technical support, particularly beamline scientist Kiyofumi Nitta. L. D. gratefully acknowledges financial support from the Swedish Energy Agency (contract 2020-005246). Y. C. and D. O. S. are grateful to the Faraday Institution for funding the MICHAEL computing cluster hosted at University College London (UCL). The calculations have been also carried out on the Thomas (Thomas@UCL) and Young (Young@UCL) High Performance Computing Facility provisioned by UCL. *Via* our membership of the UKs HEC Materials Chemistry Consortium, which is funded by EPSRC (EP/L000202, EP/R029431), this work used the ARCHER2 UK National Supercomputing Service (http://www.archer2.ac.uk). We are also grateful to the UK Materials and Molecular Modelling Hub for computational resources, which is partially funded by EPSRC (EP/P020194/1 and EP/T022213/1). We are grateful to the Engineering and Physical Sciences Research Council (EPSRC) Light Element Facility Grant (EP/T019298/1) for funding the acquisition of the Raman spectrometer. EF is grateful for an EaStCHEM studentship. This work was supported by the Faraday Institution (grant number FIRG018).

References

1 J. Y. Hwang, S. T. Myung and Y. K. Sun, *Chem. Soc. Rev.*, 2017, **46**, 3529–3614.
2 N. Yabuuchi, K. Kubota, M. Dahbi and S. Komaba, *Chem. Rev.*, 2014, **114**, 11636–11682.
3 Y. Li, Y. Lu, C. Zhao, Y. S. Hu, M. M. Titirici, H. Li, X. Huang and L. Chen, *Energy Storage Mater.*, 2017, **7**, 130–151.
4 C. Fang, Y. Huang, W. Zhang, J. Han, Z. Deng, Y. Cao and H. Yang, *Adv. Energy Mater.*, 2016, **6**, 1–18.
5 J. Do, I. Kim, H. Kim and Y. Jung, *Energy Storage Mater.*, 2020, **25**, 62–69.
6 N. Tapia-ruiz, A. R. Armstrong, H. Alptekin, M. A. Amores, H. Au, J. Barker, R. Boston, W. R. Brant, J. M. Brittain, Y. Chen, M. Chhowalla, Y. Choi, S. I. R. Costa, M. C. Ribadeneyra, S. A. M. Dickson, E. I. Eweka, J. D. Forero-saboya, C. P. Grey, Z. Li, S. F. L. Mertens, R. Mogensen, L. Monconduit, D. M. C. Ould, R. G. Palgrave, P. Poizot, A. Ponrouch, S. Renault, E. M. Reynolds, A. Rudola, R. Sayers, D. O. Scanlon, S. Sen, V. R. Seymour, B. Silv, G. S. Stone, C. I. Thomas, M. Titirici, J. Tong, T. J. Wood, D. S. Wright and R. Younesi, *J. Phys.: Energy*, 2021, **3**, 031503.
7 G. Assat and J. M. Tarascon, *Nat. Energy*, 2018, **3**, 373–386.
8 M. Sathiya, G. Rousse, K. Ramesha, C. P. Laisa, H. Vezin, M. T. Sougrati, M. L. Doublet, D. Foix, D. Gonbeau, W. Walker, A. S. Prakash, M. Ben Hassine, L. Dupont and J. M. Tarascon, *Nat. Mater.*, 2013, **12**, 827–835.
9 N. Yabuuchi, M. Takeuchi, M. Nakayama, H. Shiiba, M. Ogawa, K. Nakayama, T. Ohta, D. Endo, T. Ozaki, T. Inamasu, K. Sato and S. Komaba, *Proc. Natl. Acad. Sci. U. S. A.*, 2015, **112**, 7650–7655.
10 H. Koga, L. Croguennec, M. Ménétrier, K. Douhil, S. Belin, L. Bourgeois, E. Suard, F. Weill and C. Delmas, *J. Electrochem. Soc.*, 2013, **160**, A786–A792.
11 H. Koga, L. Croguennec, M. Ménétrier, P. Mannessiez, F. Weill and C. Delmas, *J. Power Sources*, 2013, **236**, 250–258.
12 K. Luo, M. R. Roberts, R. Hao, N. Guerrini, D. M. Pickup, Y. S. Liu, K. Edström, J. Guo, A. V. Chadwick, L. C. Duda and P. G. Bruce, *Nat. Chem.*, 2016, **8**, 684–691.
13 C. J. Chen, W. K. Pang, T. Mori, V. K. Peterson, N. Sharma, P. H. Lee, S. H. Wu, C. C. Wang, Y. F. Song and R. S. Liu, *J. Am. Chem. Soc.*, 2016, **138**, 8824–8833.
14 B. Xu, C. R. Fell, M. Chi and Y. S. Meng, *Energy Environ. Sci.*, 2011, **4**, 2223–2233.
15 W. E. Gent, K. Lim, Y. Liang, Q. Li, T. Barnes, S. J. Ahn, K. H. Stone, M. McIntire, J. Hong, J. H. Song, Y. Li, A. Mehta, S. Ermon, T. Tyliszczak, D. Kilcoyne, D. Vine, J. H. Park, S. K. Doo, M. F. Toney, W. Yang, D. Prendergast and W. C. Chueh, *Nat. Commun.*, 2017, **8**, 1–12.
16 P. Rozier, M. Sathiya, A. R. Paulraj, D. Foix, T. Desaunay, P. L. Taberna, P. Simon and J. M. Tarascon, *Electrochem. Commun.*, 2015, **53**, 29–32.
17 B. Mortemard De Boisse, G. Liu, J. Ma, S. I. Nishimura, S. C. Chung, H. Kiuchi, Y. Harada, J. Kikkawa, Y. Kobayashi, M. Okubo and A. Yamada, *Nat. Commun.*, 2016, **7**, 1–9.
18 B. Mortemard de Boisse, M. Reynaud, J. Ma, J. Kikkawa, S.-i. Nishimura, M. Casas-Cabanas, C. Delmas, M. Okubo and A. Yamada, *Nat. Commun.*, 2019, **10**, 2185.
19 U. Maitra, R. A. House, J. W. Somerville, N. Tapia-Ruiz, J. G. Lozano, N. Guerrini, R. Hao, K. Luo, L. Jin, M. A. Pérez-Osorio, F. Massel, D. M. Pickup, S. Ramos, X. Lu, D. E. McNally, A. V. Chadwick, F. Giustino, T. Schmitt, L. C. Duda, M. R. Roberts and P. G. Bruce, *Nat. Chem.*, 2018, **10**, 288–295.
20 R. A. House, U. Maitra, M. A. Pérez-Osorio, J. G. Lozano, L. Jin, J. W. Somerville, L. C. Duda, A. Nag, A. Walters, K. J. Zhou, M. R. Roberts and P. G. Bruce, *Nature*, 2020, **577**, 502–508.
21 B. Mortemard de Boisse, S.-i. Nishimura, E. Watanabe, L. Lander, A. Tsuchimoto, J. Kikkawa, E. Kobayashi, D. Asakura, M. Okubo and A. Yamada, *Adv. Energy Mater.*, 2018, **8**, S1–S7.
22 B. Song, M. Tang, E. Hu, O. J. Borkiewicz, K. M. Wiaderek, Y. Zhang, N. D. Phillip, X. Liu, Z. Shadike, C. Li, L. Song, Y. Y. Hu, M. Chi, G. M. Veith, X. Q. Yang, J. Liu, J. Nanda, K. Page and A. Huq, *Chem. Mater.*, 2019, **31**, 3756–3765.
23 Y. Li, X. Wang, Y. Gao, Q. Zhang, G. Tan, Q. Kong, S. Bak, G. Lu, X. Q. Yang, L. Gu, J. Lu, K. Amine, Z. Wang and L. Chen, *Adv. Energy Mater.*, 2019, **9**, 1–9.
24 A. Tsuchimoto, X. Shi, K. Kawai, B. M. De Boisse, J. Kikkawa, D. Asakura, M. Okubo and A. Yamada, *Nat. Commun.*, 2021, **12**, 1–7.
25 E. Adamczyk and V. Pralong, *Chem. Mater.*, 2017, **29**, 4645–4648.

26 H. Yoshida, N. Yabuuchi, K. Kubota, I. Ikeuchi, A. Garsuch, M. Schulz-Dobrick and S. Komaba, *Chem. Commun.*, 2014, **50**, 3677–3680.
27 C. Li, C. Zhao, B. Hu, W. Tong, M. Shen and B. Hu, *Chem. Mater.*, 2020, **32**, 1054–1063.
28 S. Guo, J. Yi, Y. Sun and H. Zhou, *Energy Environ. Sci.*, 2016, **9**, 2978–3006.
29 Y. Liu, C. Wang, M. Ren, H. Fang, Z. Jiang and F. Li, *J. Energy Chem.*, 2021, **63**, 351–357.
30 E. J. Kim, L. A. Ma, D. M. Pickup, A. V. Chadwick, R. Younesi, P. Maughan, J. T. S. Irvine and A. R. Armstrong, *ACS Appl. Energy Mater.*, 2020, **3**, 10423–10434.
31 E. J. Kim, L. A. Ma, L. C. Duda, D. M. Pickup, A. V. Chadwick, R. Younesi, J. T. S. Irvine and A. Robert Armstrong, *ACS Appl. Energy Mater.*, 2020, **3**, 184–191.
32 E. J. Kim, K. Mofredj, D. M. Pickup, A. V. Chadwick, J. T. S. Irvine and A. R. Armstrong, *J. Power Sources*, 2021, **481**, 229010.
33 R. D. Shannon, *Acta Crystallogr., Sect. A: Cryst. Phys., Diffr., Theor. Gen. Crystallogr.*, 1976, **32**, 751–767.
34 W. Zhao, A. Tanaka, K. Momosaki, S. Yamamoto, F. Zhang, Q. Guo and H. Noguchi, *Electrochim. Acta*, 2015, **170**, 171–181.
35 X. Cao, X. Li, Y. Qiao, M. Jia, F. Qiu, Y. He, P. He and H. Zhou, *ACS Energy Lett.*, 2019, **4**, 2409–2417.
36 K. Tang, Y. Huang, X. Xie, S. Cao, L. Liu, H. Liu, Z. Luo, Y. Wang, B. Chang, H. Shu and X. Wang, *Chem. Eng. J.*, 2020, **399**, 125725.
37 B. Zhang, B. Zhang, L. Wang, X. Chen, Y. Lu, B. Xu and W. Yang, *J. Alloys Compd.*, 2020, **824**, 153938.
38 J. H. Stansby, W. M. Dose, N. Sharma, J. A. Kimpton, J. M. López del Amo, E. Gonzalo and T. Rojo, *Electrochim. Acta*, 2020, **341**, 1–9.
39 D. Pahari and S. Puravankara, *J. Power Sources*, 2020, **455**, 227957.
40 S. Bao, S.-h. Luo, Z.-y. Wang, S.-x. Yan and Q. Wang, *J. Colloid Interface Sci.*, 2019, **544**, 164–171.
41 J. K. Park, G. G. Park, H. H. Kwak, S. T. Hong and J. W. Lee, *ACS Omega*, 2017, **3**, 361–368.
42 J.-P. Parant, R. Olazcuaga, M. Devalette, C. Fouassier and P. Hagenmuller, *J. Solid State Chem.*, 1971, **3**, 1–11.
43 D. Asakura, E. Hosono, Y. Nanba, H. Zhou, J. Okabayashi, C. Ban, P. A. Glans, J. Guo, T. Mizokawa, G. Chen, A. J. Achkar, D. G. Hawthron, T. Z. Regier and H. Wadati, *AIP Adv.*, 2016, **6**, 035105.
44 J. Lee, J. K. Papp, R. J. Clément, S. Sallis, W. Yang, B. D. Mccloskey, G. Ceder, D. Kwon and T. Shi, *Nat. Commun.*, 2017, **8**, 1–10.
45 K. Luo, M. R. Roberts, N. Guerrini, N. Tapia-Ruiz, R. Hao, F. Massel, D. M. Pickup, S. Ramos, Y. S. Liu, J. Guo, A. V. Chadwick, L. C. Duda and P. G. Bruce, *J. Am. Chem. Soc.*, 2016, **138**, 11211–11218.
46 M. Okubo and A. Yamada, *ACS Appl. Mater. Interfaces*, 2017, **9**, 36463–36472.
47 M. Tang, A. Dalzini, X. Li, X. Feng, P. H. Chien, L. Song and Y. Y. Hu, *J. Phys. Chem. Lett.*, 2017, **8**, 4009–4016.
48 M. Sathiya, J. B. Leriche, E. Salager, D. Gourier, J. M. Tarascon and H. Vezin, *Nat. Commun.*, 2015, **6**, 1–7.
49 R. Stoyanova, M. Gorova and E. Zhecheva, *J. Phys. Chem. Solids*, 2000, **61**, 615–620.
50 Q. Li, Y. Qiao, S. Guo, K. Jiang, Q. Li, J. Wu and H. Zhou, *Joule*, 2018, **2**, 1134–1145.
51 X. Li, Y. Qiao, S. Guo, Z. Xu, H. Zhu, X. Zhang, Y. Yuan, P. He, M. Ishida and H. Zhou, *Adv. Mater.*, 2018, **30**, 2–7.
52 Y. Qiao, S. Guo, K. Zhu, P. Liu, X. Li, K. Jiang, C. J. Sun, M. Chen and H. Zhou, *Energy Environ. Sci.*, 2018, **11**, 299–305.
53 D. O. Scanlon, C. W. Dunnill, J. Buckeridge, S. A. Shevlin, A. J. Logsdail, S. M. Woodley, C. R. A. Catlow, M. J. Powell, R. G. Palgrave, I. P. Parkin, G. W. Watson, T. W. Keal, P. Sherwood, A. Walsh and A. A. Sokol, *Nat. Mater.*, 2013, **12**, 798–801.
54 J. Buckeridge, K. T. Butler, C. R. A. Catlow, A. J. Logsdail, D. O. Scanlon, S. A. Shevlin, S. M. Woodley, A. A. Sokol and A. Walsh, *Chem. Mater.*, 2015, **27**, 3844–3851.
55 J. Vinckeviciute, D. A. Kitchaev and A. Van Der Ven, *Chem. Mater.*, 2021, **33**, 1625–1636.
56 E. Gonzalo, M. Zarrabeitia, N. E. Drewett, J. M. López del Amo and T. Rojo, *Energy Storage Mater.*, 2021, **34**, 682–707.
57 M. D. Radin and A. Van Der Ven, *Chem. Mater.*, 2016, **28**, 7898–7904.
58 K. S. Pitzer, *J. Am. Chem. Soc.*, 1960, **82**, 4121.
59 C. Zhao, Q. Wang, Z. Yao, J. Wang, B. Sánchez-Lengeling, F. Ding, X. Qi, Y. Lu, X. Bai, B. Li, H. Li, A. Aspuru-Guzik, X. Huang, C. Delmas, M. Wagemaker, L. Chen and Y. S. Hu, *Science*, 2020, **370**, 708–712.